Atomistic study of hydrogen embrittlement of grain boundaries in Nickel: II. Decohesion

A. Tehranchi, W. A. Curtin

Laboratory for Multiscale Mechanics Modeling, EPFL, CH-1015 Lausanne, Switzerland

Abstract. Atomistic simulations of bicrystal samples containing a grain boundary are used to examine the effect of hydrogen atoms on the nucleation of intergranular cracks in Ni. Specifically, the theoretical strength is obtained by rigid separation of the two crystals above and below the GB and the yield strength (point of dislocation emission) is obtained by standard tension testing normal to the GB. These strengths are computed in pure Ni and Ni with H segregated to the grain boundaries under conditions typical of H embrittlement in Ni, and in highly-H-saturated states. In all GBs studied here, the theoretical strength $\hat{\sigma}$ is not significantly reduced by the presence of the hydrogen atoms. Similarly, with the exception of the $\mathrm{Ni}\Sigma27(115)\langle110\rangle$ boundary, the yield strength σ_y is not significantly altered by the presence of segregated H atoms. In all cases, the theoretical strengths are ~25 GPa and the yield strengths are ~10 GPa, so that (i) the theoretical strength is always well above the yield strength, with or without H, and (ii) both strengths are far above the bulk plastic flow stress, $\sigma_\mathrm{y}^\mathrm{B}$ of Ni and Ni alloys. Complementing recent work showing that H does not change the ability of GB cracks to emit dislocations and blunt, the present work indicates that hydrogen atoms segregated to the GB have little effect on lowering the GB strength and so do not significantly facilitate nucleation of intergranular cracks.

Keywords: Theoretical strength, Yield strength, dislocation emission, Grain boundary, Hydrogen embrittlement

1. Introduction

It is well-established that hydrogen degrades the mechanical properties of metals [1, 2, 3, 4, 5, 6]. Hydrogen embrittlement (HE), where the ductility of the host metal is significantly decreased by the presence of hydrogen atoms, is a major problem in many current applications of high-performance metals and so is receiving considerable research attention. Although experiments clearly demonstrate embrittlement, the microscopic processes are not established nor does a comprehensive and predictive theory for this phenomenon yet exist. Atomic-scale simulations are thus increasingly being used to test possible embrittlement concepts [7, 8, 9, 10, 11, 12, 13, 14, 15, 16], within the limitations of such modeling. Since embrittlement is often accompanied by a change from ductile fracture to intergranular cleavage, mechanisms involving H segregation at grain boundaries would seem to be of particular importance.

There are two coupled phenomena involved in possible embrittlement at a grain boundary: crack nucleation and crack growth. These processes could occur quasi-statically or dynamically, introducing a possible time dependence into the phenomena. An additional time dependence occurs if H can diffuse into grain boundaries or toward grain boundary crack tips within the time scale of the mechanical loading [14, 15]. In the present work, we do not consider explicit long-range H diffusion during the mechanical testing, and only consider H pre-segregated to the grain boundaries. Several material properties then control the crack nucleation and growth phenomena. The first property of interest is the grain boundary tensile strength under cleavage-like separation. Complicating the concept of tensile strength of a grain boundary is the fact that grain boundary can emit dislocations under tensile load, which dissipates energy and precludes purely cleavage-like separation. The second property of interest is the brittle cleavage fracture energy, which is the difference between the intact grain boundary and the fractured system wherein two free surfaces near/along the grain boundary are present. The third property of interest is the propensity for crack-tip dislocation emission, which is a mechanism of crack blunting and, thus, prevention of cleavage.

In the absence of H, most metals do not fail by intergranular cleavage, consistent with the high toughness of metals. Generally, the grain boundary tensile strength is much higher than the typical plastic flow strength of the bulk metal, $\sigma_\mathrm{y}^\mathrm{B}$, and under tension loading the grain boundary will emit dislocations prior to any cleavage-like separation. During bulk plastic deformation, dislocations will impinge on the grain boundaries, inducing local structural disorder, and dislocation pile-ups could generate high local stresses, but these phenomena evidently do not lead to crack nucleation under monotonic loading. Furthermore, cracks placed along the grain boundary will generally emit dislocations, at least for many orientations of the crack front, thus preventing large-scale crack growth. In the presence of H segregated to the grain boundary, all of the above properties could be

changed, and these changes could possibly lead to a change from "ductile" fracture behavior that does not involve grain boundary fracture to "brittle" intergranular failure.

In recent work, we have investigated the behavior of cracks along GBs in Ni, with and without H, using molecular statics simulations. These studies show that, while H can influence the applied load levels at which crack-tip phenomena occur, there is little evidence for embrittlement (i.e. a change in the crack behavior from dislocation emission and blunting to cleavage-like failure). Those results suggest that embrittlement would require, at least, some additional H transport to GBs above the equilibrium segregation values at typical conditions of embrittlement in Ni. In any case, crack tip studies do not address the origins of such cracks, and it is possible that embrittlement occurs via facilitated nucleation of cracks, which may form and grow dynamically such that blunting and other plasticity processes are suppressed. Therefore, in this paper, we examine the tensile failure behavior of representative GBs in Ni, with and without segregated H, to draw conclusions about crack nucleation. We find that segregated H has negligible influence on (i) the tensile stress at which dislocations are nucleated from the GB, (ii) the "cohesive strength" or maximum strength under rigid separation across various potential fracture planes, or (iii) the fracture energy after complete separation of the GBs. Furthermore, for Ni, the stress levels at dislocation nucleation and at decohesion exceed 10 GPa and 20 GPa, respectively, which are far above any bulk stresses reached in Ni or its alloys. Between the present work and the complementary work on crack behavior, we thus find no evidence for H embrittlement at GBs in Ni under conditions of fixed segregation of H to the Ni GBs. These results thus imply that H transport is necessary to drive embrittlement, consistent with at least one mechanism proposed in the literature [14, 15].

The remainder of this paper is organized as follows. The interaction energies and segregation of H to atomic sites in a range of symmetric tilt boundaries in Ni are presented in Section 2. Section 3 summarizes the details of simulations of the theoretical and yield strengths, and fracture energies, with and without H segregated to all the GBs considered here. Results are presented in section 4, and discussion of the results is provided in Section 5.

2. Energetics of H atoms in Ni symmetric tilt boundaries

H atoms occupy octahedral interstitial sites in bulk Ni, but their binding energies to sites in and around grain boundaries depend on the atomistic structure of each specific boundaries [17]. For a possible binding site i, the interaction energy of H relative to the energy of H in a bulk octahedral site is defined as

$$E_{\text{int,i}} = E_i^{\text{GB+H}} - E_{\text{bulk}}^{\text{GB+H}} \tag{1}$$

where $E_i^{\text{GB+H}}$ is the energy of a fully-relaxed material containing a grain boundary with an H atom at site $\#i$ and where $E_{\text{bulk}}^{\text{GB+H}}$ is the energy of the same fully-relaxed material with an H atom in a bulk interstitial site far from the GB. To compute all energies, we used our recently-improved EAM potential for the Ni-H system, which is described in Ref. [18]. We study the following grain boundaries: $\text{Ni}\Sigma9(221)\langle110\rangle$, $\text{Ni}\Sigma19(331)\langle110\rangle$, $\text{Ni}\Sigma27(115)\langle110\rangle$, $\text{Ni}\Sigma33a(441)\langle110\rangle$, $\text{Ni}\Sigma33b(554)\langle110\rangle$, $\text{Ni}\Sigma41(443)\langle110\rangle$ and $\text{Ni}\Sigma99(557)\langle110\rangle$. Fig. 1 shows the positions of the binding sites for H (defined as $E_{\text{int,i}} < -0.05\ eV$) in each GB with the corresponding interaction energies shown in Table 1. In all cases, the H atoms tend to bind to sites having a more open structure [17], due to the positive misfit volume of the H interstitial atom in Ni. We have further verified that H–H interactions in nearby binding sites are negligible. Therefore, we compute the probability of occupation c_i of sites of type i, which we refer to as the concentration at site i, using a simple solution model as

$$c_i = \frac{c_0 \exp(-E_{\text{int},i}/k_B T)}{1 + c_0 \exp(-E_{\text{int},i}/k_B T)}. \tag{2}$$

Here, T is the temperature and k_B is Boltzmann's constant, while c_0 is the bulk concentration of H atoms which corresponds to some imposed H chemical potential for the entire specimen. These concentrations c_i are used for preparing the simulation specimens as described in the next section.

Table 1: Interaction energies for hydrogen atoms at various sites in $Ni\Sigma9(221)\langle110\rangle$, $Ni\Sigma19(331)\langle110\rangle$, $Ni\Sigma27(115)\langle110\rangle$, $Ni\Sigma33a(441)\langle110\rangle$, $Ni\Sigma33b(554)\langle110\rangle$, $Ni\Sigma41(443)\langle110\rangle$, $Ni\Sigma99(557)\langle110\rangle$ as predicted by the modified EAM potential.

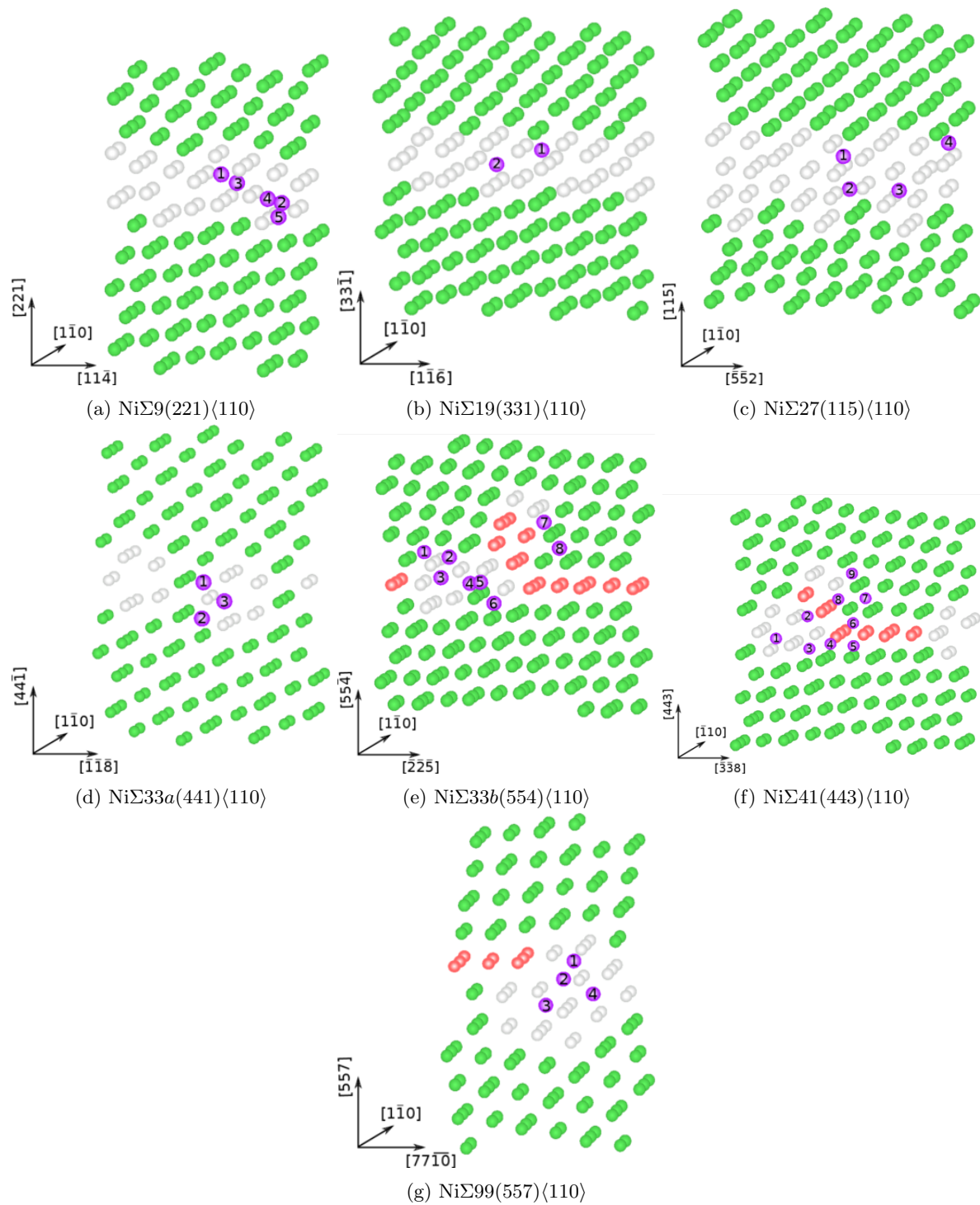|	$E_{int}(eV)$						
# site	$Ni\Sigma9(221)\langle110\rangle$	$Ni\Sigma19(331)\langle110\rangle$	$Ni\Sigma27(115)\langle110\rangle$	$Ni\Sigma33a(441)\langle110\rangle$	$Ni\Sigma33b(554)\langle110\rangle$	$Ni\Sigma41(443)\langle110\rangle$	$Ni\Sigma99(557)\langle110\rangle$
1	-0.20	-0.15	-0.11	-0.25	-0.11	-0.18	-0.15
2	-0.16	-0.22	-0.19	-0.25	-0.14	-0.27	-0.20
3	-0.16	-	-0.20	-0.25	-0.19	-0.25	-0.26
4	-0.20	-	-0.10	-	-0.18	-0.22	-0.21
5	-0.16	-	-	-	-0.15	-0.18	-
6	-	-	-	-	-0.20	-0.25	-
7	-	-	-	-	-0.19	-0.25	-
8	-	-	-	-	-0.14	-0.14	-
9	-	-	-	-	-	-0.22	-

Figure 1: Structure and hydrogen binding sites in various symmetric tilt boundaries: (a) NiΣ9(221)⟨110⟩; (b) NiΣ19(331)⟨110⟩; (c) NiΣ27(115)⟨110⟩; (d) NiΣ33a(441)⟨110⟩; (e) NiΣ33b(554)⟨110⟩; (f)NiΣ41(443)⟨110⟩; (g) NiΣ99(557)⟨110⟩. Atoms colored by Common Neighbor Analysis (Green: fcc Ni; Red: hcp Ni; White: Ni with less than 12 neighbors; Purple: H binding sites)

3. Simulation details

In this section, the details of the simulations pertinent to the calculation of the theoretical cohesive strength $\hat{\sigma}$, the fracture energies γ_{fr}, and the grain boundary yield strength σ_{y} of the various grain boundaries are presented.

We examine the effect of the hydrogen atoms on the theoretical strength of various grain boundaries as follows. We construct simulation cells of size $l_1 \in [200\text{Å}, 260\text{Å}]$, $l_2 \in [209\text{Å}, 211\text{Å}]$ and $l_3 = 12.4\text{Å}$ containing a GB (NiΣ9(221)⟨110⟩, NiΣ19(331)⟨110⟩, NiΣ27(115)⟨110⟩, NiΣ33a(441)⟨110⟩, NiΣ33b(554)⟨110⟩, NiΣ41(443)⟨110⟩ or NiΣ99(557)⟨110⟩) along the central plane $x_2 = 0$. The simulation cells are periodic in x_1 and x_3 directions and have free boundaries in the x_2 direction. We note that grain boundaries have an intrinsic

stress. Therefore, in a finite size sample that is fully relaxed to zero net stress in all directions, this intrinsic GB stress is balanced by a compensating stress in the two grains on either side of the boundary. This compensating stress decreases with increasing height l_2 of the sample and would vanish in a large-grain sample. To avoid spurious effects of this compensating stress in finite-size MD samples, we fixing the l_1 width of the sample at the size corresponding to the bulk Ni lattice constant, and the Ni grains are under zero stress while the GB stress is also appropriate to the bulk value.

After proper relaxation of the specimen, we saturate the binding sites of the grain boundaries with hydrogen atoms due to the concentrations c_i calculated via by inserting interaction energies calculated in the previous section into Eq. (2). The bulk concentration of hydrogen is set to $c_0 = 0.001$, typical of embrittlement conditions in Ni at T=300K [19]. For each GB we prepare H-charged samples at both $T = 300K$ and $T = 50K$. The latter low temperature gives rise to $c_i > 0.994$ for all binding sites that are not also nearly fully occupied at $T = 300K$. Thus, in the low-T sample, the H concentrations in the GB are nearly fully-saturated, and independent of c_0, thus representing a highly-charged system. After insertion of the H atoms in the binding sites, we relax the system again to mechanical equilibrium at $T = 0K$ (maintaining the fixed l_1 sample length, however). Since the barrier for the diffusion of hydrogen atoms in fcc nickel is ~ 0.5eV, H diffusion cannot be captured in molecular dynamics (MD) timescales at $T = 300K$. Moreover, we are not concerned with any thermally activated process here. Therefore, we execute all simulations at T=0K.

Starting from the relaxed boundary, we rigidly separate the two grains across a specified plane parallel to the grain boundary as schematically shown in Fig. 2. We measure the interfacial stress σ_{22} as a function of the planar separation distance δ, up to $\delta = 10$Å at which point the stress is always zero (beyond the range of the EAM potential).

The unrelaxed fracture energy $\gamma_{\mathrm{fr}}^{\mathrm{u}}$ is the difference between the initial and final system energies, with no relaxation during the rigid separation process, divided by the GB area. The $\gamma_{\mathrm{fr}}^{\mathrm{u}}$ is exactly equal to the work done in the separation process, which corresponds to the area under the measured stress-opening (σ_{22}–δ) curve. We then allow full relaxation of the separated surfaces to obtain the relaxed fracture energy $\gamma_{\mathrm{fr}}^{\mathrm{r}}$; this is the relevant energy in the equilibrium Griffith criterion for cleavage crack growth along the selected plane of separation with no H diffusion. Several possible separation planes are chosen for each GB so as to find the *minimum* cohesive strength and *minimum* fracture energy surfaces for each GB. For each GB, three different cutting planes P_i $(i = 1, 2, 3)$ are chosen shown in Figures 4–10.
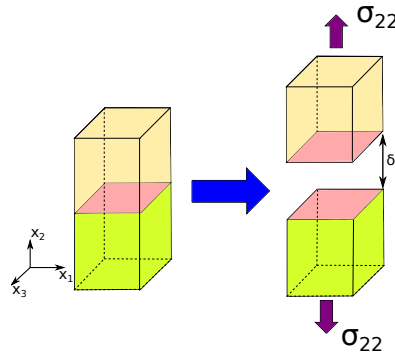

Figure 2: Schematic diagram of the rigid grain boundary seperation process.

To measure the yield strength of the GB, we use the same initial specimens those used for the cohesive strength and fracture energy studies above. All GBs studied here have slip planes with normal vectors in the x_1, x_2 plane, and so are able to emit straight dislocations consistent with the periodic boundary conditions imposed in x_3. The specimen is subjected to an increasing strain tensor corresponding to an increasing uniaxial stress, in increments of $\Delta\boldsymbol{\epsilon} = \mathbf{C}^{-1}\Delta\boldsymbol{\sigma}$ where $\mathbf{C}$ is the elastic stiffness tensor calculated with respect to x_i coordinate system and

$$\Delta\boldsymbol{\sigma} = \begin{pmatrix} \sigma_{11} & \sigma_{12} & \sigma_{13} \\ \sigma_{21} & \sigma_{22} & \sigma_{23} \\ \sigma_{31} & \sigma_{32} & \sigma_{33} \end{pmatrix} = \begin{pmatrix} 0 & 0 & 0 \\ 0 & 200 & 0 \\ 0 & 0 & 0 \end{pmatrix} \text{MPa}. \tag{3}$$

Since we are simulating $\langle 110 \rangle$ symmetric tilt boundaries in fcc, the stress field is symmetric with respect to the GB plane ($x_2 = 0$). We thus do not need to solve the general aniostropic elasticity problem for tension of a bi-material to find $\Delta\boldsymbol{\epsilon}$. After each load increment, the specimen is relaxed via the conjugate gradient method [20]. We measure the GB yield stress as that uniaxial stress at which dislocation(s) are first emitted from the grain boundary.

Furthermore, we examine the possible effects of H atoms on the plastic activity of the GB at loads higher than the initial GB yield stresses. However, previously emitted dislocations cannot be pinned at the sample

boundaries and, thus, exert improper backstresses on the GB. Therefore, in these simulations, the system is loaded by application of forces on the x_2 surfaces corresponding to desired tensile stress. Application of the forces at the free top and bottom enables the emitted dislocations exit from these free surfaces and thus exert no spurious forces that might affect subsequent emission from the GB. MD simulations are then performed using the velocity–Verlet algorithm [21] with integration time step of 1 fs. A Langevin thermostat [22] is used for fixing the temperature of the system $10^{-3}K$, so that MD is very nearly equivalent to a steepest-descent minimization. After application of the total desired load, MD is executed for t = 50 ps.

All MD and MS simulations are performed using the large-scale atomic/molecular massively parallel simulator (LAMMPS) [23] and atomic configurations are visualized using the open visualization tool OVITO [24].

4. Results

Fig. 3 shows the computed σ_{22}–δ curves for all the grain boundaries, for pure Ni, and with H at bulk concentration of $c_0 = 0.001$ at both $T = 300K$, and $T = 50K$. In each case, these curves are those for the cutting plane having the minimum theoretical cohesive strength. Table 2 shows the computed cohesive strength of each boundary. The cohesive strengths of the boundaries are not significantly altered by the presence of H atoms, with a maximum reduction of ≈ 4 percent. In addition, the strengths are all very high, on the order of 25 GPa, which is expected from simple estimates (25 GPa $\sim$E/5 where E is the Young's modulus for polycrystalline Ni). There is thus no significant effect of H on the cohesive strength of any of these GBs.

As stated before, for further investigation of the maximal role of H atoms on the theoretical strength, we prepared samples in which all the binding sites of the grain boundary were filled with hydrogen, i.e. $c_i = 1$ by setting $T = 50$ in Eq. (2). These samples are not in the thermodynamical equilibrium at room temperature but they may represent situations in which, due to local transport phenomena, the concentration of H might become high in the GB. For example dislocations carrying Cotterell clouds of hydrogen may come to the GB and provide additional H that is redistributed locally (out of global equilibrium). Even in these extreme cases, there are no significant decrease in the theoretical cohesive strength, with a maximum reduction of only 5.4%, found for the NiΣ27(115)⟨110⟩ case.

For completeness, the theoretical cohesive strength of a single Ni grain that is separated across a plane parallel to each GB has also been examined for both $c_0 = 0$ and $c_0 = 1$ (complete filling of all octahedral sites in the entire specimen), as shown in Table 3. In all of these "single crystal" orientations, the pure Ni specimens have theoretical cohesive strengths around 28 GPa, roughly 12% higher than the corresponding bicrystal specimens. The reductions in theoretical cohesive strength due to the presence of the hydrogen atoms remain small, less than 3.5%, except for Ni(115) where the reduction is 19%.

Table 2: Theoretical cohesive strengths and yield strengths of the grain boundaries of interest.

		Yield stress (GPa)						Theoretical strength (GPa)				
		$c_0 = 0$	$c_0 = 0.001$					$c_0 = 0$	$c_0 = 0.001$			
			$T = 300K$	(%)	$T = 50K$	(%)			$T = 300K$	(%)	$T = 50K$	(%)
NiΣ9(221)⟨110⟩	P_1	6.1	6.7	9.8	7.0	14.7	P_1	26.6	**26.3**	-1.1	**26.2**	-1.5
	P_2						P_2	**26.4**	26.4	0.0	26.6	0.8
	P_3						P_3	26.6	27.1	1.9	26.3	-1.1
NiΣ19(331)⟨110⟩	P_1	8.66	7.94	-8.3	10	15.5	P_1	25.4	**24.4**	-3.9	26.6	4.7
	P_2						P_2	**25.4**	24.4	-3.9	26.9	5.9
	P_3						P_3	27.9	27.1	-2.9	**26.5**	-5.0
NiΣ27(115)⟨110⟩	P_1	7.6	16.7	119.7	17.4	128.9	P_1	27.0	27.3	1.1	27.1	0.4
	P_2						P_2	27.0	27.3	1.1	27.1	0.4
	P_3						P_3	**26.1**	25.1	-3.8	**24.7**	-5.4
NiΣ33a(441)⟨110⟩	P_1	4.9	6.7	36.7	6.9	40.8	P_1	**26.4**	26.5	0.37	26.6	0.8
	P_2						P_2	26.9	26.7	-0.7	26.7	-0.7
	P_3						P_3	27.0	26.6	-1.5	**26.5**	-1.9
NiΣ33b(554)⟨110⟩	P_1	2.7	3.4	25.9	3.6	33.4	P_1	**26.2**	26.8	2.3	**26.1**	-0.4
	P_2						P_2	27.0	26.4	-2.2	26.0	-3.7
	P_3						P_3	26.5	26.5	0	27.0	1.9
NiΣ41(443)⟨110⟩	P_1	2.4	3.0	25	3.7	54.2	P_1	**26.7**	27.1	1.5	27.5	3.0
	P_2						P_2	27.5	27.1	-1.5	27.1	-1.5
	P_3						P_3	27.1	**26.9**	-0.7	**27.0**	-0.4
NiΣ99(557)⟨110⟩	P_1	11.2	13.6	21.4	13.8	23.2	P_1	26.6	27.0	1.5	**26.2**	-1.5
	P_2						P_2	**26.3**	**26.4**	0.4	26.6	1.1
	P_3						P_3	27.2	26.4	-2.9	26.3	-3.3

Table 3: Theoretical cohesive strength of single crystal Ni separated across different crystallographic planes corresponding to planes parallel to the various grain boundaries studied here, in pure Ni and Ni-H (100% occupation of octahedral sites in Ni).

	Theoretical strength (GPa)		
	$c_0 = 0$	$c_0 = 1$	change (%)
Ni(221)	28.6	28.0	-2.1
Ni(331)	27.5	27.6	0.3
Ni(115)	28.4	23.0	-19.0
Ni(441)	27.1	27.2	0.37
Ni(554)	28.6	27.7	-3.1
Ni(443)	28.5	27.7	-2.8
Ni(557)	28.6	28.0	-2.1
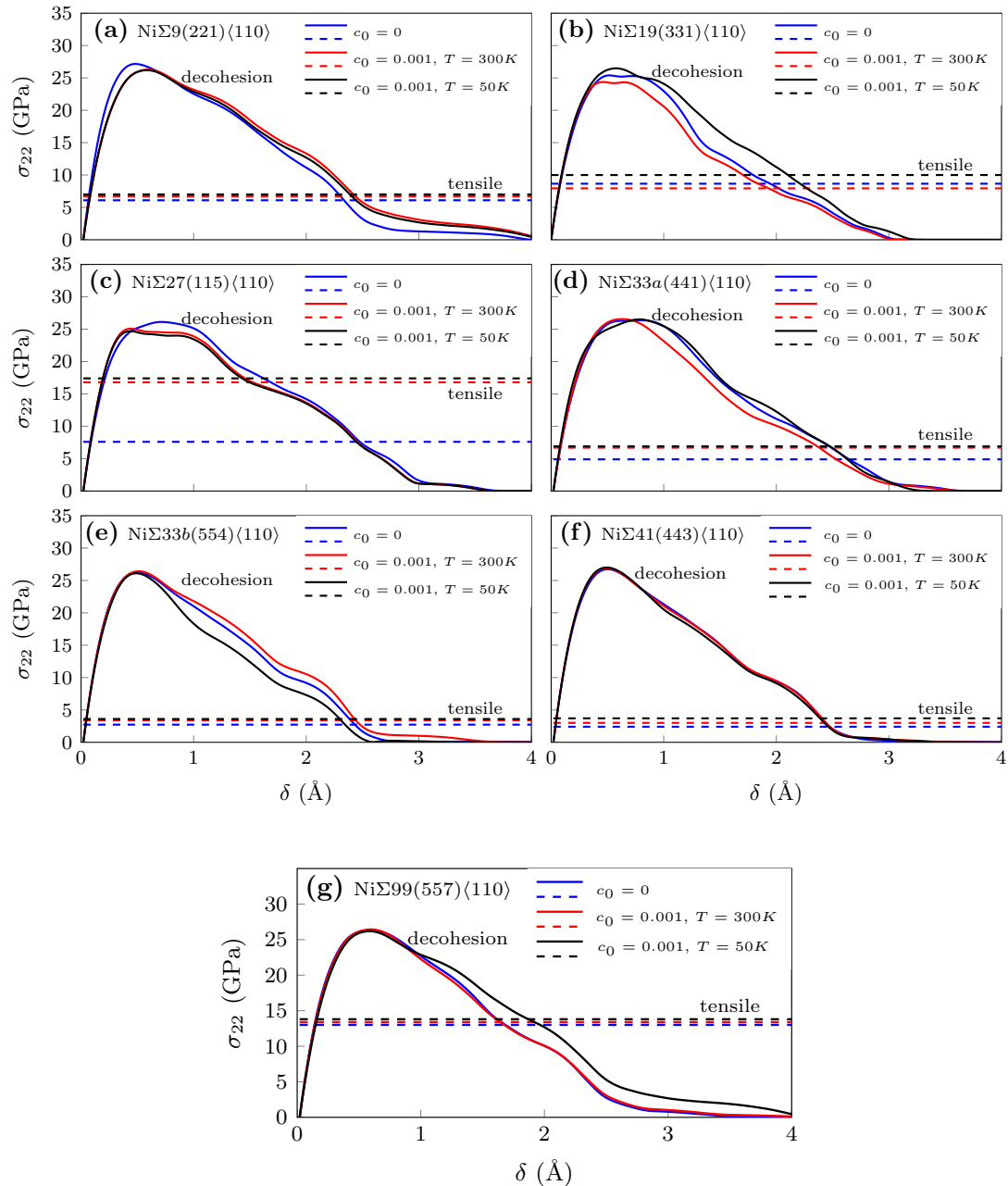
Figure 3: Normal stress versus normal displacement during rigid-block separation across the minimum strength cleavage plane, with and without H, and for a range of grain boundary structures.

The unrelaxed and relaxed fracture energies calculated for each grain boundary and each plane of separation are shown in Table 4. Relaxation reduces the minimum fracture energy by 21% and 23% in the H-free and

Table 4: Unrelaxed and fully relaxed fracture energies (mJ/m^2) for the separation of GBs along different possible fracture planes. The minimum separation energy for each GB is highlighted in bold.

		$c_0 = 0$			$c_0 = 0.001$			$c_0 = 0.001$(local diffusion)	
		γ_{fr}^u	γ_{fr}^r	reduction (%)	γ_{fr}^u	γ_{fr}^r	reduction (%)	γ_{fr}^r	reduction (%)
	P_1	**3625**	3438	5	**3562**	**3377**	4.9	3377	0
NiΣ9(221)⟨110⟩	P_2	4482	3437	23	4462	3384	24.1	3384	0
	P_3	4753	**3427**	27	4745	3437	27	3370	1.9
	P_1	3940	3589	8.9	**3674**	3254	11.5	3254	0
NiΣ19(331)⟨110⟩	P_2	**3940**	**3589**	8.9	3677	**3254**	11.6	3254	0
	P_3	4886	3589	26.5	4732	3547	25	**3135**	11.6
	P_1	**4305**	3464	19.5	4131	3649	11.7	3483	4.5
NiΣ27(115)⟨110⟩	P_2	4312	**3462**	19.7	**4131**	3649	11.7	**3483**	4.5
	P_3	4823	3479	28	4665	3862	17.2	3582	7.2
	P_1	**4252**	3426	19.4	**4576**	4073	11	3273	19.6
NiΣ33a(441)⟨110⟩	P_2	4376	**3396**	22.4	4800	**3724**	22.4	3019	18.9
	P_3	4823	3479	28	4665	3862	22.8	3028	21.6
	P_1	**3857**	3314	14.1	**3655**	3104	15.1	**3055**	1.6
NiΣ33b(554)⟨110⟩	P_2	4236	3476	18	4175	3358	19	3274	2.5
	P_3	4059	**3306**	18.5	3979	3257	18	**2935**	9.9
	P_1	**3942**	3238	17.8	**3667**	**2932**	20	2482	15.3
NiΣ41(443)⟨110⟩	P_2	4159	**3238**	22.5	3922	3008	23	**2482**	17.5
	P_3	4121	3310	19.7	3980	3557	10.6	2482	30.2
	P_1	4378	3718	15.1	4853	3801	21	3787	0.5
NiΣ99(557)⟨110⟩	P_2	**4162**	**3273**	21.3	**4170**	**3191**	23	**3162**	0.9
	P_3	4475	3756	16	4484	3541	21	3515	0.7

H-charged cases, respectively. Moreover, the presence of H atoms does not significantly reduce the unrelaxed nor relaxed minimum fracture energy of any grain boundary. The maximum reduction due to H is 10%, obtained for NiΣ41(443)⟨110⟩. Interestingly, the relaxed fracture energy is slightly increased due to the presence of H atoms in NiΣ27(115)⟨110⟩ and NiΣ33a(441)⟨110⟩ because the H atoms are not on the separated surfaces. In general, when H atoms are not on the "fracture surface", we can envision rapid nanoscale diffusion, due to both a reduction in energy and a short diffusion distance, that transports H to the fracture surfaces. We have thus manually moved all subsurface H atoms to the separated surfaces and calculated the relaxed fracture energy; the computed configurations are shown in Figs. 4–10. This nanoscale diffusion does decrease in γ_{fr}^r but the reductions in fracture energy due to segregated H remain less than 25%. Table 4 summarizes all of these results. By of these simulations, we conclude that the presence of hydrogen, even in conjunction with local diffusion processes bringing nearby H to the fracture surfaces, does not significantly change the fracture energies of any of the grain boundaries studied here.
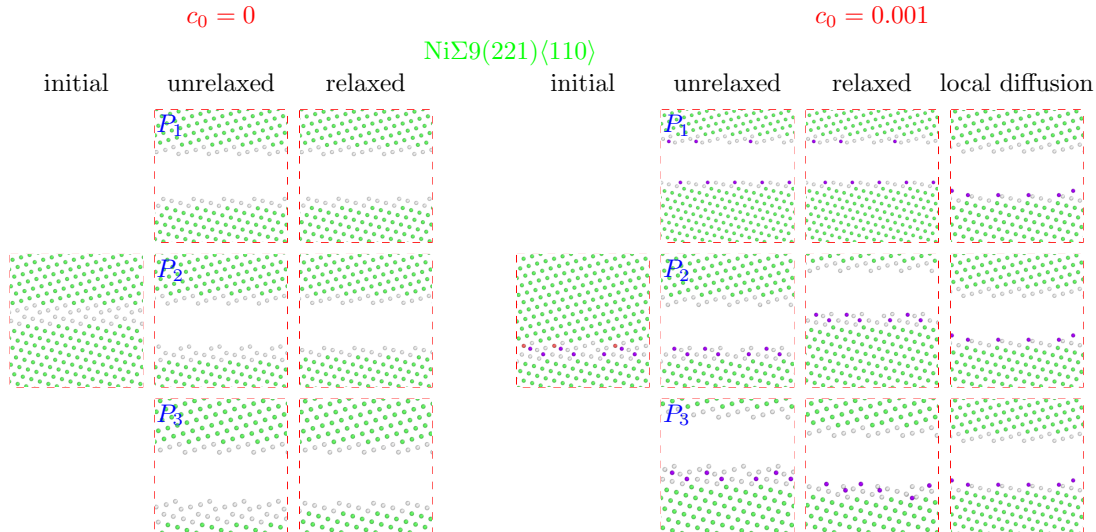

Figure 4: Atomic configurations of NiΣ9(221)⟨110⟩. For each grain boundary, the relaxed and unrelaxed configuration of the separated grains through three different cutting planes are given. Atoms colored by Common Neighbor Analysis (Green: fcc Ni; Red: hcp Ni; White: Ni with less than 12 neighbors; Purple: H)
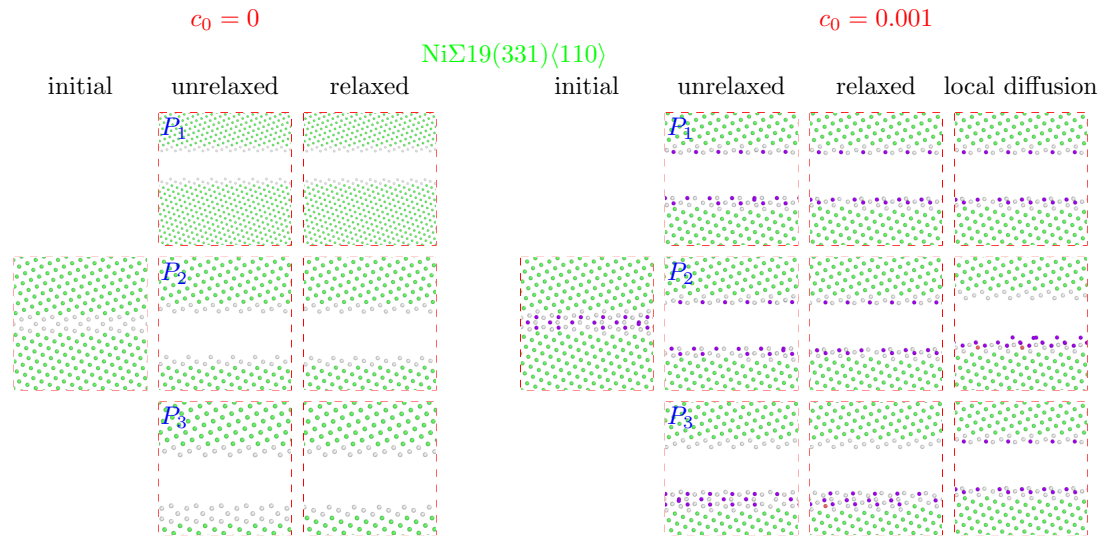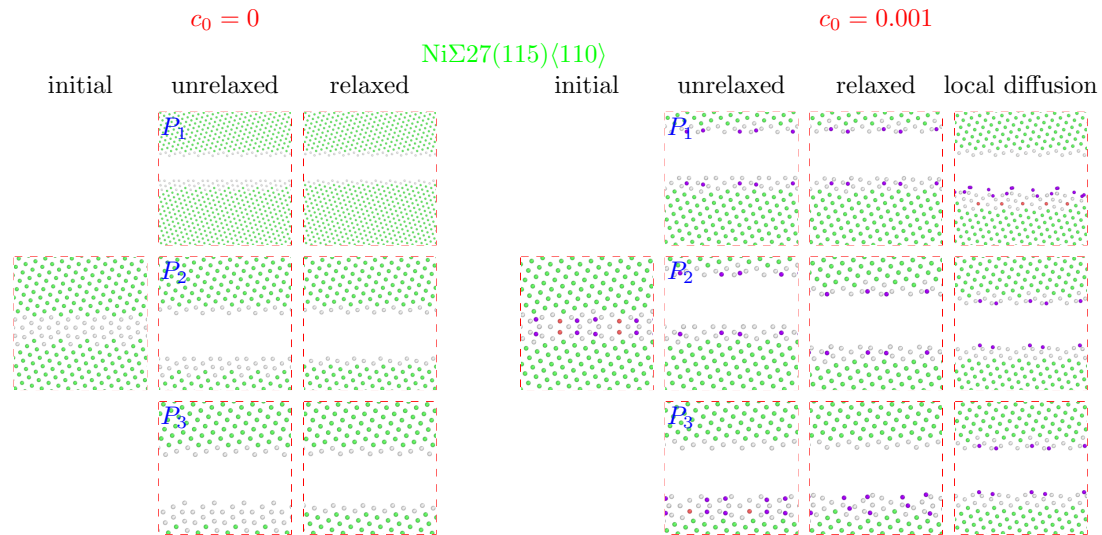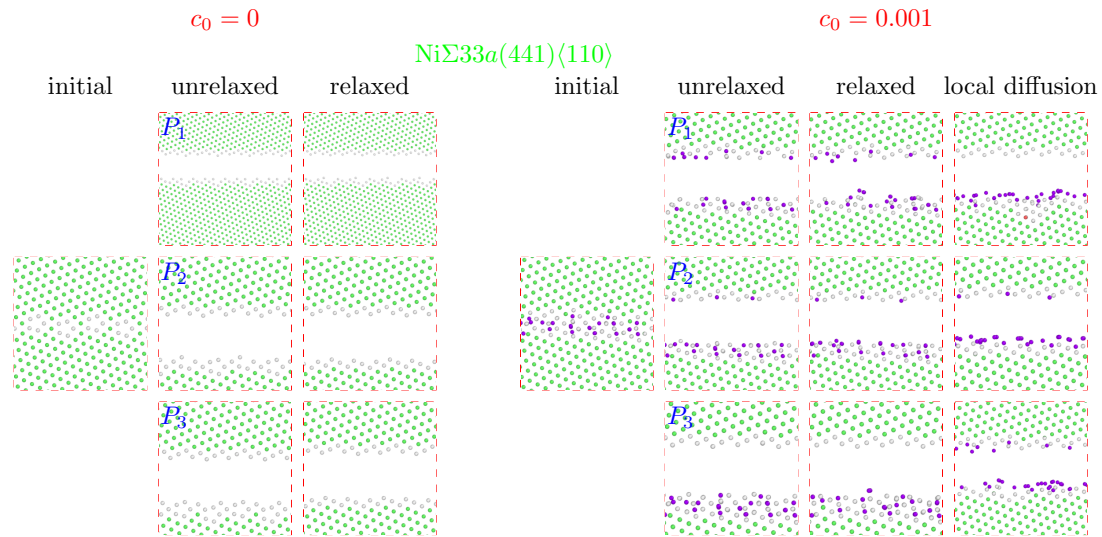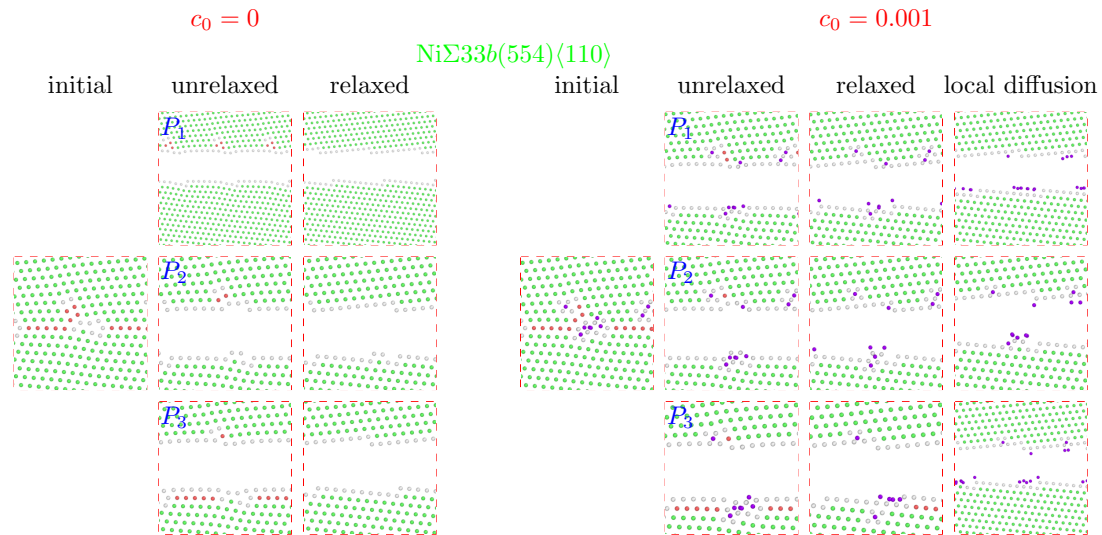
Figure 5: Atomic configurations of NiΣ19(331)⟨110⟩. For each grain boundary, the relaxed and unrelaxed configuration of the separated grains through three different cutting planes are given. Atoms colored by Common Neighbor Analysis (Green: fcc Ni; Red: hcp Ni; White: Ni with less than 12 neighbors; Purple: H)
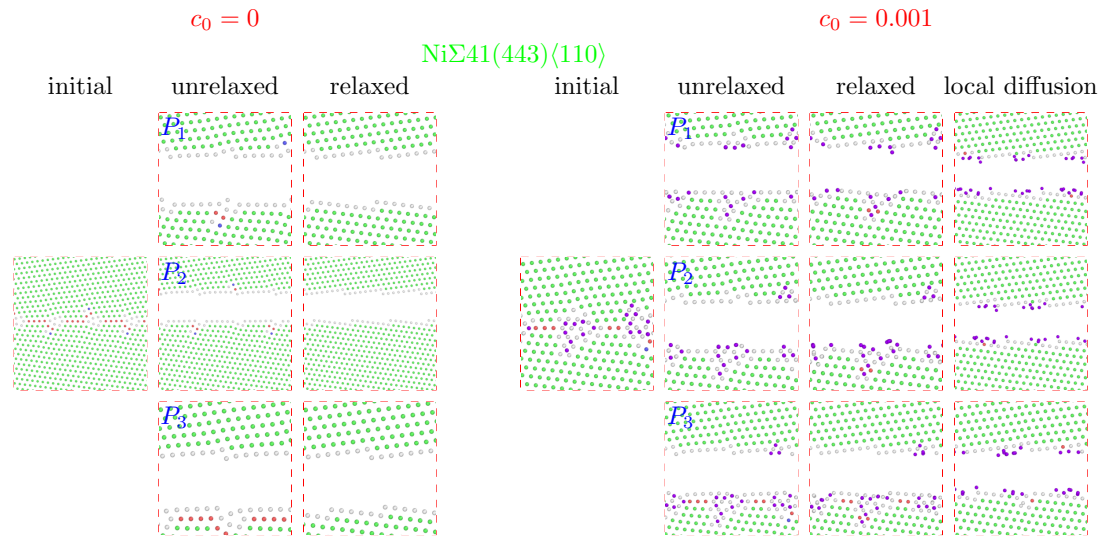

Figure 6: Atomic configurations of NiΣ27(115)⟨110⟩. For each grain boundary, the relaxed and unrelaxed configuration of the separated grains through three different cutting planes are given. Atoms colored by Common Neighbor Analysis (Green: fcc Ni; Red: hcp Ni; White: Ni with less than 12 neighbors; Purple: H)
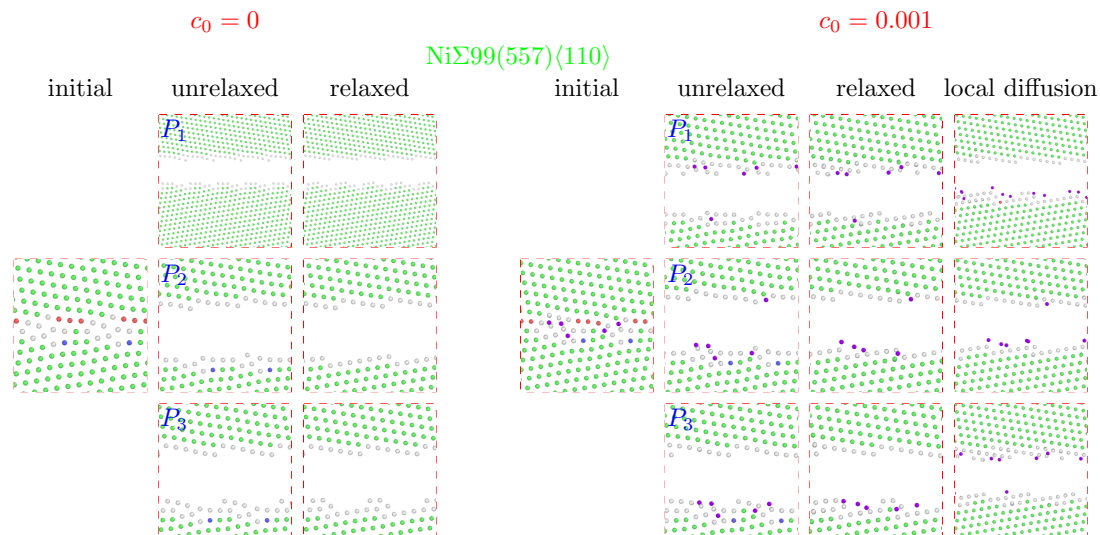
Figure 7: Atomic configurations of NiΣ33a(441)⟨110⟩. For each grain boundary, the relaxed and unrelaxed configuration of the separated grains through three different cutting planes are given. Atoms colored by Common Neighbor Analysis (Green: fcc Ni; Red: hcp Ni; White: Ni with less than 12 neighbors; Purple: H)

Figure 8: Atomic configurations of NiΣ33b(554)⟨110⟩. For each grain boundary, the relaxed and unrelaxed configuration of the separated grains through three different cutting planes are given. Atoms colored by Common Neighbor Analysis (Green: fcc Ni; Red: hcp Ni; White: Ni with less than 12 neighbors; Purple: H)

Figure 9: Atomic configurations of NiΣ41(443)⟨110⟩. For each grain boundary, the relaxed and unrelaxed configuration of the separated grains through three different cutting planes are given. Atoms colored by Common Neighbor Analysis (Green: fcc Ni; Red: hcp Ni; White: Ni with less than 12 neighbors; Purple: H)

Figure 10: Atomic configurations of NiΣ99(557)⟨110⟩. For each grain boundary, the relaxed and unrelaxed configuration of the separated grains through three different cutting planes are given. Atoms colored by Common Neighbor Analysis (Green: fcc Ni; Red: hcp Ni; White: Ni with less than 12 neighbors; Purple: H)

(a) $\sigma_{22} = 6.1 GPa$ (b) $\sigma_{22} = 6.7 GPa$ (c) $\sigma_{22} = 15 GPa$
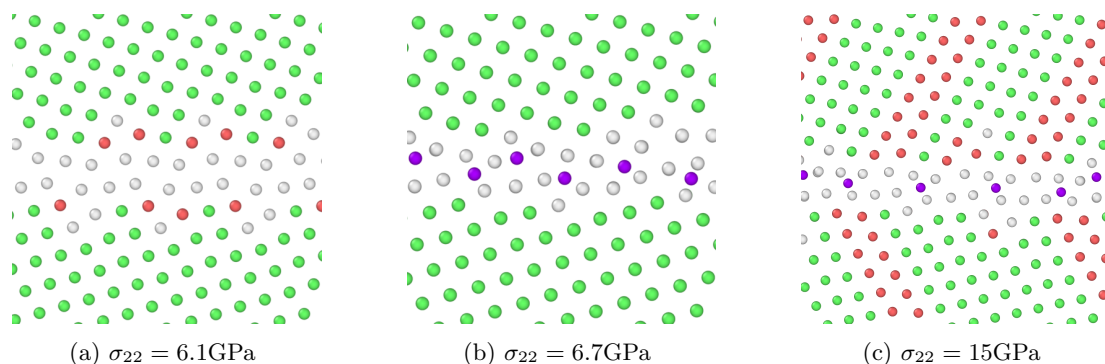
Figure 11: Key atomic configurations of (a) H-free and (b) H-charged NiΣ9(221)⟨110⟩ at room temperature, at the onset of the first plastic activity. (c) Configuration of the H-charged specimen subjected to tensile stress of $\sigma_{22} = 15 GPa$. Atoms colored by Common Neighbor Analysis (Green: fcc Ni; Red: hcp Ni; White: Ni with less than 12 neighbors; Purple: H)

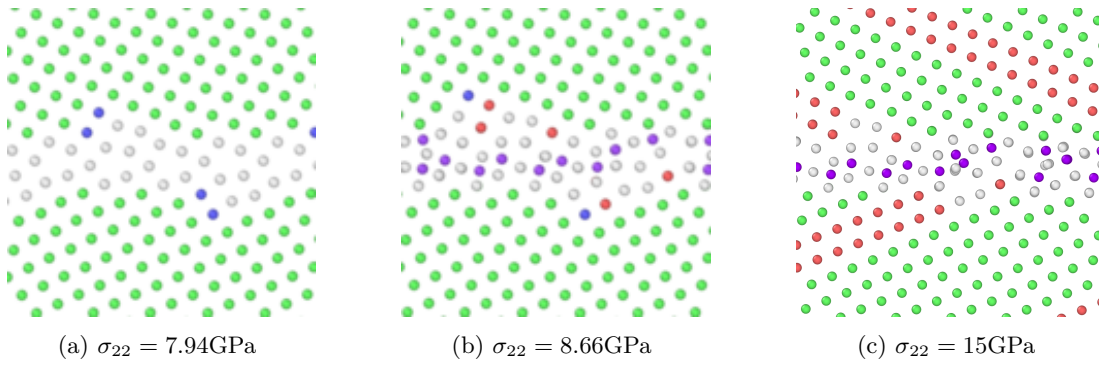| (a) $\sigma_{22} = 7.94$GPa | (b) $\sigma_{22} = 8.66$GPa | (c) $\sigma_{22} = 15$GPa |

Figure 12: Key atomic configurations of (a) H-free and (b) H-charged NiΣ19(331)$\langle$110$\rangle$ at room temperature, at the onset of the first plastic activity. (c) Configuration of the H-charged specimen subjected to tensile stress of $\sigma_{22} = 15GPa$. Atoms colored by Common Neighbor Analysis (Green: fcc Ni; Red: hcp Ni; White: Ni with less than 12 neighbors; Purple: H)


| (a) $\sigma_{22} = 7.6$GPa | (b) $\sigma_{22} = 16.7$GPa | (c) $\sigma_{22} = 20$GPa |
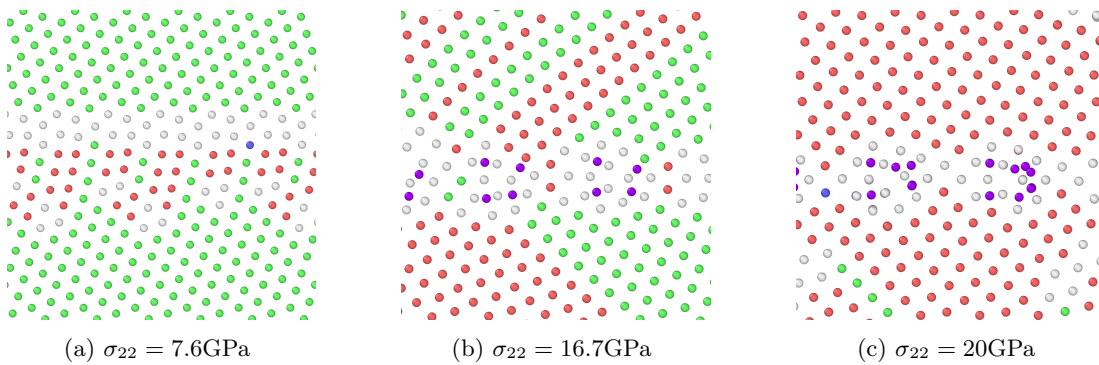
Figure 13: Key atomic configurations of (a) H-free and (b) H-charged NiΣ27(115)$\langle$110$\rangle$ at room temperature, at the onset of the first plastic activity. (c) Configuration of the H-charged specimen subjected to tensile stress of $\sigma_{22} = 20GPa$. Atoms colored by Common Neighbor Analysis (Green: fcc Ni; Red: hcp Ni; White: Ni with less than 12 neighbors; Purple: H)

| (a) $\sigma_{22} = 4.9$GPa | (b) $\sigma_{22} = 6.7$GPa | (c) $\sigma_{22} = 15$GPa |
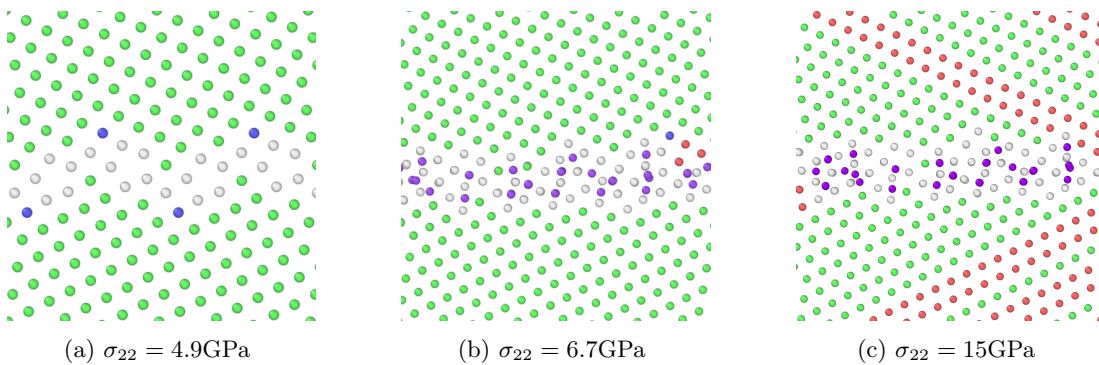
Figure 14: Key atomic configurations of (a) H-free and (b) H-charged NiΣ33(441)$\langle$110$\rangle$ at room temperature, at the onset of the first plastic activity. (c) Configuration of the H-charged specimen subjected to tensile stress of $\sigma_{22} = 15GPa$. Atoms colored by Common Neighbor Analysis (Green: fcc Ni; Red: hcp Ni; White: Ni with less than 12 neighbors; Purple: H)

(a) $\sigma_{22} = 2.7$GPa   (b) $\sigma_{22} = 3.4$GPa   (c) $\sigma_{22} = 15$GPa
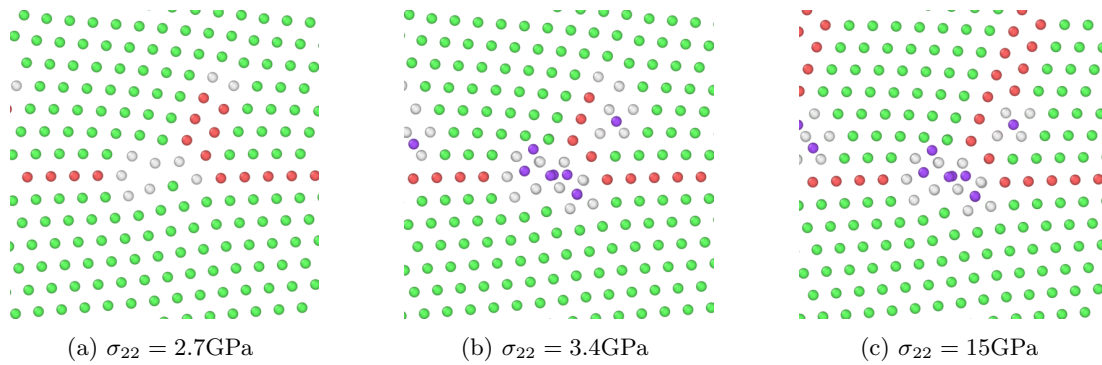
Figure 15: Key atomic configurations of (a) H-free and (b) H-charged NiΣ33b(554)$\langle$110$\rangle$ at room temperature, at the onset of the first plastic activity. (c) Configuration of the H-charged specimen subjected to tensile stress of $\sigma_{22} = 15GPa$. Atoms colored by Common Neighbor Analysis (Green: fcc Ni; Red: hcp Ni; White: Ni with less than 12 neighbors; Purple: H)
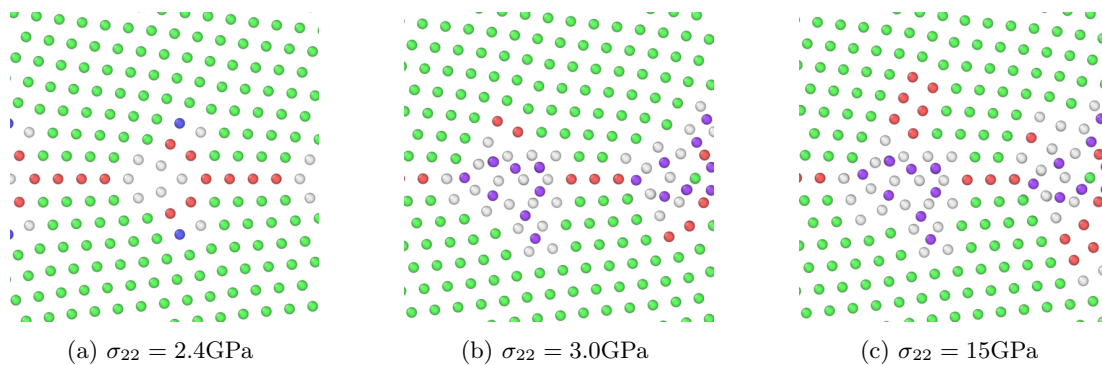

(a) $\sigma_{22} = 2.4$GPa   (b) $\sigma_{22} = 3.0$GPa   (c) $\sigma_{22} = 15$GPa

Figure 16: Key atomic configurations of (a) H-free and (b) H-charged NiΣ41(443)$\langle$110$\rangle$ at room temperature, at the onset of the first plastic activity. (c) Configuration of the H-charged specimen subjected to tensile stress of $\sigma_{22} = 15GPa$. Atoms colored by Common Neighbor Analysis (Green: fcc Ni; Red: hcp Ni; White: Ni with less than 12 neighbors; Purple: H)
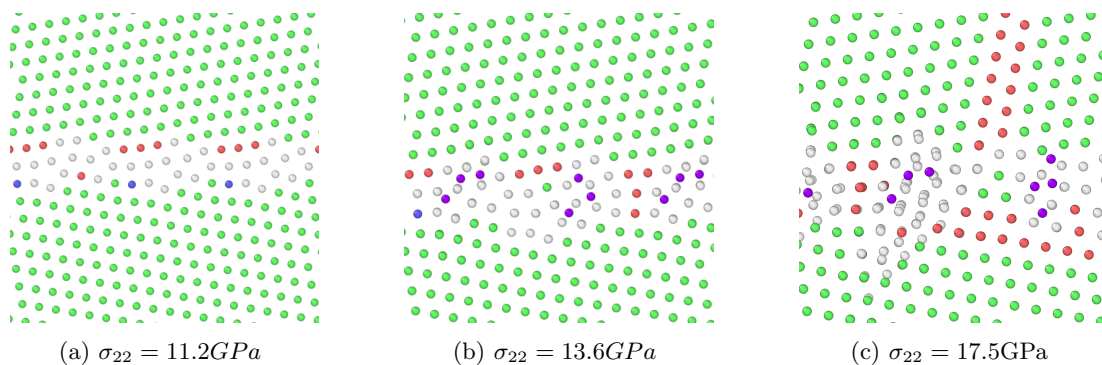

(a) $\sigma_{22} = 11.2GPa$ (b) $\sigma_{22} = 13.6GPa$ (c) $\sigma_{22} = 17.5$GPa

Figure 17: Key atomic configurations of (a) H-free and (b) H-charged NiΣ99(557)$\langle$110$\rangle$ at room temperature, at the onset of the first plastic activity. (c) Configuration of the H-charged specimen subjected to tensile stress of $\sigma_{22} = 17.5GPa$. Atoms colored by Common Neighbor Analysis (Green: fcc Ni; Red: hcp Ni; White: Ni with less than 12 neighbors; Purple: H)

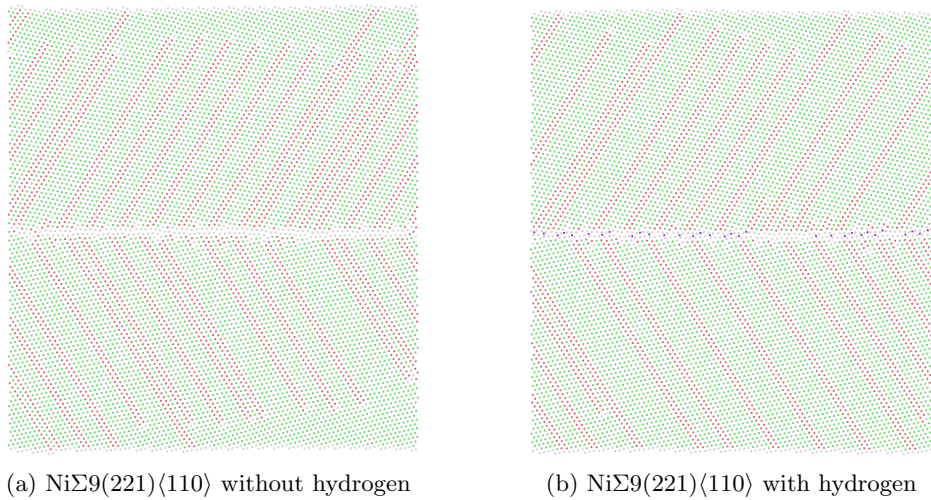(a) NiΣ9(221)⟨110⟩ without hydrogen   (b) NiΣ9(221)⟨110⟩ with hydrogen

Figure 18: (a) H-free and (b) H-charged specimenes containing NiΣ9(221)⟨110⟩ at room temperature, subjected to $\sigma_{22} = 15GPa$. Atoms colored by Common Neighbor Analysis (Green: fcc Ni; Red: hcp Ni; White: Ni with less than 12 neighbors; Purple: H))

(a) NiΣ33b(554)⟨110⟩ without hydrogen   (b) NiΣ33b(554)⟨110⟩ with hydrogen
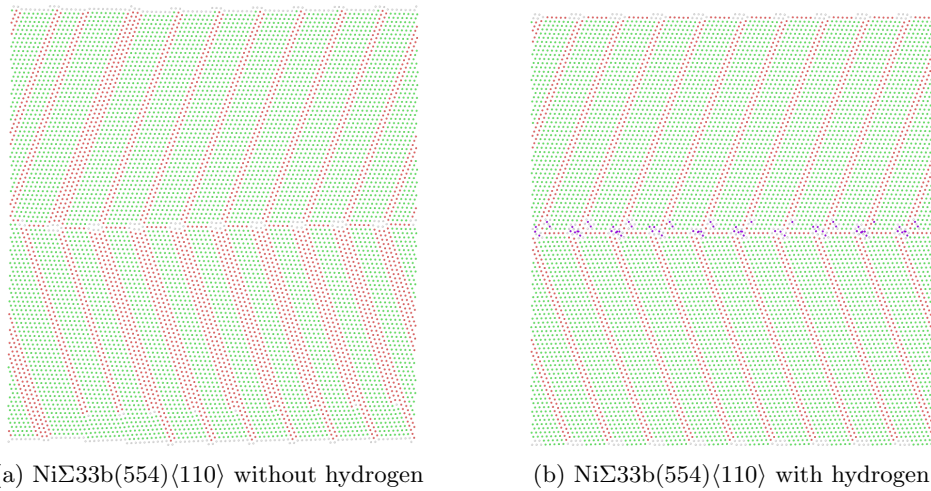
Figure 19: (a) H-free and (b) H-charged specimenes containing NiΣ33b(554)⟨110⟩ at room temperature, subjected to $\sigma_{22} = 15GPa$. Atoms colored by Common Neighbor Analysis (Green: fcc Ni; Red: hcp Ni; White: Ni with less than 12 neighbors; Purple: H)

We now turn to results for the GB "yield strength" under uniaxial tensile load. We consider grain boundaries with no H, with segregated H at $c_0 = 0.001$ and $T = 300K$, and with saturated H wherein all binding sites are filled independent of any thermodynamic considerations at room temperature. All grain boundaries show dislocation emission at some tensile stress that is well below the theoretical cohesive strength, as shown by the dashed lines in Figure 3. In no cases do we find any crack nucleation or evidence of decohesion prior to dislocation emission. Furthermore, the presence of H has very little effect on the stress at which dislocation emission occurs, except in one case NiΣ27(115)⟨110⟩ where dislocation emission is significantly suppressed but still occurring well below the theoretical cohesive strength. The details of the dislocation emission vary from GB to GB, but the emphasis here is on when dislocation emission occurs and whether the emission is affected by segregated H. Figures 11–17, show the atomic GB structures at the first points of GB reorganization, both with and without H. These results show that dislocation emission is the preferred response of each GB under tensile load, which is expected since intergranular fracture is not observed in pure Ni, and that H has no significant influence on the stress levels at which emission occurs.

Furthermore, all the grain boundaries with and without hydrogen continue emitting dislocation as the loading levels increase above the initial yield stress. Figures 11(c)–17(c) show the structure around the GBs with segregated hydrogen atoms under tensile stresses higher than the yield stress. For NiΣ27(115)⟨110⟩, and NiΣ99(557)⟨110⟩ boundaries, the applied tensile stresses in the Figure are $\sigma_{22} = 20GPa$ and $\sigma_{22} = 17.5GPa$, respectively, while for all other boundaries the stress in the Figure is $\sigma_{22} = 15GPa$. Figures 18–19 show structure of the entire specimen, for the NiΣ9(221)⟨110⟩ and NiΣ33b(554)⟨110⟩ under $\sigma_{22} = 15GPa$ at $t = 50ps$,

respectively. The emitted dislocations exit the top and bottom surfaces, which are thus roughened. Extensive
twinning can be seen, which is not necessarily physical but the point is that there is no crack nucleation.

5. Discussion

In all simulations reported here, the fracture energies and theoretical cohesive strengths of the boundaries are not significantly reduced by the presence of the hydrogen atoms. Furthermore, in all cases, the emission of dislocations occurs well before decohesion. And, aside from the case of Ni$\Sigma 27(115)\langle 110\rangle$, no significant change in σ_y is observed in the H-charged specimens. Thus we find little or no evidence that segregated hydrogen atoms can facilitate the nucleation of the cracks along GBs in Ni under conditions where embrittlement is typically observed in experiments. Below we discuss different features and implications of this conclusion.

The main material parameter controlling nucleation of a crack is the theoretical cohesive strength $\hat{\sigma}$. If the tensile stress somewhere along the GB can reach $\hat{\sigma}$, a crack can nucleate. After nucleation, if the local stress field remains high, the energy release rate may be well above both the fracture energy for cleavage and the unstable stacking fault energy (γ_{usf}) for dislocation emission. Although recent simulation studies suggest otherwise [25], a crack could then grow dynamically under such high-stress conditions rather than blunt out and stop. As the crack grows longer, the applied stress intensity can increase even when the overall applied stresses are decreasing as the crack tips move away from the original high-stress nucleation point, and this could allow crack growth to continue. At present, however, our nanoscale assessment of fracture behavior is mainly limited to quasistatic situations, with cleavage and blunting governed by the Griffith (fracture energy) and Rice [26] (unstable stacking fault energy) criteria, respectively. And, as alluded to above, recent simulations show that when a dynamic cleavage crack enters a material that is quasistatically ductile (emits dislocations under quasistatic loading) then the dynamic crack emits dislocations and stops growing. Thus, based on quasistatic considerations, our analysis here and in our earlier work shows that the presence of H along symmetric tilt grain boundaries in Ni does not significantly change either the cohesive strength, fracture energy, or induce a change from emission to cleavage at a crack front. Thus, the nanoscale mechanisms of crack nucleation and growth at GBs are similar in Ni and Ni-H. Ni itself does not show intergranular fracture, and hence results here do not point to the creation of intergranular fracture due to pre-segregated H to GBs in Ni. These analyses are at the nanoscale. One might put aside nanoscale details in favor of a larger-scale analysis of fracture, as discussed next.

The role of H could be to inhibit or change mechanisms of ductile failure, e.g. H could change the plastic flow behavior of the bulk matrix so as to inhibit void nucleation, growth, and/or coalescence. Recent experiments in steels suggest that, in the presence of H, nanovoids are formed along GBs and that coalescence of these nanovoids could lead to embrittlement fracture along grain boundaries [27]. Mechanisms for this behavior remain to be uncovered, however [28, 29].

Another large-scale perspective assumes some effective crack tip cohesive behavior, which represents all of the complex nano/micro scale phenomena that exists along with the bulk plasticity of the surrounding metal. Numerical simulations of such cohesive cracks growing through power-law-plasticity metals show that the steady-state toughness enhancement due to plasticity, Γ/γ_{fr}, depends sensitively on the ratio $\hat{\sigma}/\sigma_y^B$ [30, 31] and on the power-law hardening rate N. If the introduction of H could decrease $\hat{\sigma}$ and/or γ_{fr} or increase σ_y^B, then the macroscopic toughness Γ could decrease substantially if the ratio $\hat{\sigma}/\sigma_y^B$ decreases below $\sim 3-5$. The nanoscale material parameters here suggest $\hat{\sigma}/\sigma_y^B \sim 15-40$, both with and without H along the GBs, so that cohesive cracks in a power-law plastic matrix should not be embrittled. However, the increase in plastic flow stress in small volumes and/or under high strain or stress gradients around crack tips leads to much higher flow stresses at the micron-scale, which facilitates fracture [31, 32, 33, 34]. In specific numerical studies, crack propagation becomes possible for larger ratios of $\hat{\sigma}/\sigma_y^B$. For instance, the Discrete Dislocation Dynamics simulations show crack growth for $\hat{\sigma}/\sigma_y^B \sim 10-12$. However, the toughness varies much more smoothly with $\hat{\sigma}/\sigma_y^B$ than in standard size-independent plasticity models so that no abrupt embrittlement would be anticipated for modest changes in material properties. Plastic flow is also rate-dependent, with increasing plastic flow stress σ_y^B with increasing strain rate, and this could affect fracture [35, 36, 37]. Rate-dependent flow could thus reduce $\hat{\sigma}/\sigma_y^B$ further, corresponding to lower predicted fracture toughness. However, both rate- and size-effects should operate for H-free materials (e.g. pure Ni or Ni alloys), and such materials are not low-toughness. The modest effects of H segregated to GBs (modest decreases in cohesive strength and fracture energy) that are caused here by H segregation to grain boundaries do not suggest significant embrittlement effects even when larger-scale phenomena are considered.

It may be useful to combine all of the effects noted above (rate- and size-dependent plasticity; reductions in cohesive strength and fracture energy due to H) into appropriate computational models so as to quantitatively assess the total effects of segregated H on toughening. This would be especially useful if the presence of H could lead to crack nucleation that creates a dynamic situation that would not prevail in the absence of H. Such computations neglect, however, the blunting of cracks by dislocation emission that should inhibit embrittlement, and the origin of easier crack nucleation in the presence of H is not indicated by the present results.

In summary, the present results, and complementary recent work [18], on the effects of H segregation to grain boundaries in Ni show no noticeable propensity for H to induce significant embrittlement in Ni. These results are time-independent, and thus do not consider H transport. A recent model by one of the present authors [14, 15] suggests that H transport to the region around an existing crack tip can suppress dislocation emission and consequent blunting, thereby preserving a sharp crack and enabling cleavage failure. Estimates of embrittlement in Ni using this model are consistent with experimental trends, including reduced embrittlement in materials engineered to contain more twin boundaries, but are not yet quantitative. Experiments are also mixed regarding time dependence, with some embrittlement being explicitly time-dependent and other reports of embrittlement at low temperatures (e.g. 77K) where H transport should be very slow. Thus, the mechanisms of H embrittlement, even in a relatively simple metal like fcc Ni where experimental evidence is abundant, remain open for discovery.

Acknowledgments

References

[1] R. N. Iyer, H. W. Pickering, Mechanism and kinetics of electrochemical hydrogen entry and degradation of metallic systems, Annual Review of Materials Science 20 (1) (1990) 299–338.

[2] S. M. Myers, M. Baskes, H. Birnbaum, J. W. Corbett, G. DeLeo, S. Estreicher, E. E. Haller, P. Jena, N. M. Johnson, R. Kirchheim, et al., Hydrogen interactions with defects in crystalline solids, Reviews of Modern Physics 64 (2) (1992) 559.

[3] H. Vehoff, Hydrogen related material problems, in: Hydrogen in metals III, Springer, 1997, pp. 215–278.

[4] S. Lynch, Mechanisms of hydrogen assisted cracking-a review, Hydrogen Effects on Material Behaviour and Corrosion Deformation Interactions (2003) 449–466.

[5] R. P. Gangloff, Hydrogen assisted cracking of high strength alloys, Tech. rep., DTIC Document (2003).

[6] A. Pundt, R. Kirchheim, Hydrogen in metals: microstructural aspects, Annu. Rev. Mater. Res. 36 (2006) 555–608.

[7] M. Wen, Z. Li, A. Barnoush, Atomistic study of hydrogen effect on dislocation nucleation at crack tip, Advanced Engineering Materials 15 (11) (2013) 1146–1151.

[8] S. Taketomi, R. Matsumoto, N. Miyazaki, Atomistic study of the effect of hydrogen on dislocation emission from a mode ii crack tip in alpha iron, International Journal of Mechanical Sciences 52 (2) (2010) 334–338.

[9] R. Matsumoto, S. Taketomi, S. Matsumoto, N. Miyazaki, Atomistic simulations of hydrogen embrittlement, international journal of hydrogen energy 34 (23) (2009) 9576–9584.

[10] Z. Hu, S. Fukuyama, K. Yokogawa, S. Okamoto, Hydrogen embrittlement of a single crystal of iron on a nanometre scale at a crack tip by molecular dynamics, Modelling and Simulation in Materials Science and Engineering 7 (4) (1999) 541.

[11] X. Xu, M. Wen, Z. Hu, S. Fukuyama, K. Yokogawa, Atomistic process on hydrogen embrittlement of a single crystal of nickel by the embedded atom method, Computational materials science 23 (1) (2002) 131–138.

[12] J. von Pezold, L. Lymperakis, J. Neugebeauer, Hydrogen-enhanced local plasticity at dilute bulk h concentrations: The role of h–h interactions and the formation of local hydrides, Acta Materialia 59 (8) (2011) 2969–2980.

[13] M. Q. Chandler, M. Horstemeyer, M. Baskes, P. Gullett, G. Wagner, B. Jelinek, Hydrogen effects on nanovoid nucleation in face-centered cubic single-crystals, Acta Materialia 56 (1) (2008) 95–104.

[14] J. Song, W. A. Curtin, A nanoscale mechanism of hydrogen embrittlement in metals, Acta Materialia 59 (4) (2011) 1557–1569.

[15] J. Song, W. A. Curtin, Atomic mechanism and prediction of hydrogen embrittlement in iron, Nature materials 12 (2) (2013) 145–151.

[16] J. Song, M. Soare, W. A. Curtin, Testing continuum concepts for hydrogen embrittlement in metals using atomistics, Modelling and Simulation in Materials Science and Engineering 18 (4) (2010) 045003.

[17] X. Zhou, D. Marchand, D. L. McDowell, T. Zhu, J. Song, Chemomechanical origin of hydrogen trapping at grain boundaries in fcc metals, Physical review letters 116 (7) (2016) 075502.

[18] A. Tehranchi, W. A. Curtin, Atomistic study of hydrogen embrittlement of grain boundaries in nickel: I. fracture, Journal of the mechanics and physics of solids (2017) Accepted.

[19] S. Bechtle, M. Kumar, B. P. Somerday, M. E. Launey, R. O. Ritchie, Grain-boundary engineering markedly reduces susceptibility to intergranular hydrogen embrittlement in metallic materials, Acta Materialia 57 (14) (2009) 4148–4157.

[20] M. Hestenes, E. Stiefel, Methods of conjugate gradients for solving linear systems, Journal of Research of the National Bureau of Standards 49 (6) (1952) 409.

[21] P. H. B. William C. Swope Hans C. Andersen, K. R. Wilson, A computer simulation method for the calculation of equilibrium constants for the formation of physical clusters of molecules: Application to small water clusters, J. Chem. Phys. 76 (1) (1982) 637–649.

[22] T. Schneider, E. Stoll, Molecular-dynamics study of a three-dimensional one-component model for distortive phase transitions, Physical Review B 17 (3) (1978) 1302–1322.

[23] S. Plimpton, Fast parallel algorithms for short-range molecular dynamics, Journal of computational physics 117 (1) (1995) 1–19.

[24] A. Stukowski, Visualization and analysis of atomistic simulation data with ovito–the open visualization tool, Modelling and Simulation in Materials Science and Engineering 18 (1) (2009) 015012.

[25] V. Rajan, W. A. Curtin, Crack tip blunting and cleavage under dynamic conditions, Journal of the Mechanics and Physics of Solids 90 (2016) 18–28.

[26] J. R. Rice, Dislocation nucleation from a crack tip: an analysis based on the peierls concept, Journal of the Mechanics and Physics of Solids 40 (2) (1992) 239–271.

[27] T. Neeraj, R. Srinivasan, J. Li, Hydrogen embrittlement of ferritic steels: observations on deformation microstructure, nanoscale dimples and failure by nanovoiding, Acta Materialia 60 (13) (2012) 5160–5171.

[28] S. Li, Y. Li, Y.-C. Lo, T. Neeraj, R. Srinivasan, X. Ding, J. Sun, L. Qi, P. Gumbsch, J. Li, The interaction of dislocations and hydrogen-vacancy complexes and its importance for deformation-induced proto nano-voids formation in α-fe, International Journal of Plasticity 74 (2015) 175–191.

[29] A. Tehranchi, X. Zhang, G. Lu, W. A. Curtin, Hydrogen–vacancy–dislocation interactions in α-fe, Modelling and Simulation in Materials Science and Engineering 25 (2) (2016) 025001.

[30] V. Tvergaard, J. W. Hutchinson, The relation between crack growth resistance and fracture process parameters in elastic-plastic solids, Journal of the Mechanics and Physics of Solids 40 (6) (1992) 1377–1397.

[31] Y. Wei, J. W. Hutchinson, Steady-state crack growth and work of fracture for solids characterized by strain gradient plasticity, Journal of the Mechanics and Physics of Solids 45 (8) (1997) 1253–1273.

[32] M. R. Begley, J. W. Hutchinson, The mechanics of size-dependent indentation, Journal of the Mechanics and Physics of Solids 46 (10) (1998) 2049–2068.

[33] S. S. Chakravarthy, W. A. Curtin, Stress-gradient plasticity, Proceedings of the National Academy of Sciences 108 (38) (2011) 15716–15720.

[34] S. Olarnrithinun, S. Chakravarthy, W. A. Curtin, Discrete dislocation modeling of fracture in plastically anisotropic metals, Journal of the Mechanics and Physics of Solids 61 (6) (2013) 1391–1406.

[35] L. Freund, J. Hutchinson, P. Lam, Analysis of high-strain-rate elastic-plastic crack growth, Engineering Fracture Mechanics 23 (1) (1986) 119–129.

[36] L. Freund, J. Hutchinson, High strain-rate crack growth in rate-dependent plastic solids, Journal of the Mechanics and Physics of Solids 33 (2) (1985) 169–191.

[37] T. Siegmund, N. Fleck, A. Needleman, Dynamic crack growth across an interface, International Journal of Fracture 85 (4) (1997) 381–402.